Version of Record: https://www.sciencedirect.com/science/article/pii/S0022311523000570
Manuscript_43dc4d71ca23761356b6a85a2ef0e8a4

An Examination of the Precipitation Behavior of Proton Irradiated Dual Phase 308L Weldment Filler Materials

Zhen Li[a]*, Xun Zhan[b], Waclaw Swiech[c], Honghui Zhou[c], Weicheng Zhong[a], Benjamin J. Sutton[d], Carly J. Romnes[a], Dhruval K. Patel[a], Nachiket S. Shah[b], and Brent J. Heuser[a]*

a) Department of Nuclear, Plasma, and Radiological Engineering, University of Illinois, Urbana, IL, 61801, USA.

b) Department of Materials Science and Engineering, University of Illinois, Urbana, IL, 61801, USA.

c) Materials Research Laboratory, University of Illinois, Urbana, IL, 61801, USA.

d) Electric Power Research Institute, Charlotte, NC, 28262, USA.

Abstract

Voids, G phase particles, and Ni-Si rich clusters in proton irradiated dual phase 308L groove filler of a SA508-304L dissimilar metal weldment are analyzed using advanced characterization techniques. These weldments are often used in light water nuclear reactors and are subject to enhanced corrosion and associated stress corrosion cracking (SCC). Radiation damage is known to accelerate SCC. Ni-Si enriched clusters were observed in proton irradiated γ austenite, while G phase $M_6Ni_{16}Si_7$ (where M transition metal element) precipitates were observed in proton irradiated δ ferrite. Compositional analysis of the G phase precipitates and Ni-Si clusters from STEM-EDS and APT are compared. Unlike G phase particles in proton irradiated δ ferrite, Ni-Si clusters in proton irradiated γ austenite are not rich in Mn. Both STEM-EDS and APT line-scan profiles of the Ni-Si clusters show that the Fe and Cr concentration gradient between matrix γ austenite and the Ni-Si clusters is not as sharp as those between matrix δ ferrite and G phase. Further, HR-STEM imaging indicates that the lattice parameter of the Ni-Si clusters is commensurate with γ austenite and the clusters do not represent the precipitation of a second phase. Our analysis demonstrates the density and volume fraction of G phase particles and the density of voids scales with proton irradiation damage and the energy to recoils.

*Corresponding author: bheuser@illinois.edu

Key words: G phase precipitation, Ni-Si clustering, proton irradiation, atom probe tomography, SA508-304L weldment, 308L groove filler.

1. Introduction

Low-alloy steel (LAS) SA508 and 300 series stainless steels find wide use in the light water reactor (LWR) nuclear power plants. Ferritic SA508 has high strength [1, 2], making this material a good choice for reactor pressure vessels (RPVs) and steam generators in the LWR systems. While the excellent corrosion resistance of 300 series stainless facilitates uses as tubing/piping in the LWR systems [3], these alloys are susceptible to both SCC and irradiation-assisted stress corrosion cracking (IASCC) [4-7]. SA508-304L dissimilar metal weldments (DMWs) are often found in nuclear power plants. The use of this DMW allowed us to study several interfaces and zones, although SA508-304L DMWs typically do not experience significant fast neutron flux. However, our focus is on the weld joint (the 308L groove filler), which is susceptible to degradation phenomenon due to residual stress [8] and unfavorable dual phase microstructural associated within the heat affected zone [8, 9]. Further, 308L and 309L both show high susceptibility to IASCC in BWR coolant environments [10]. However, only a few recent studies of irradiated dual phase 308L or 309L exist in the published literature [11-13]. 308L stainless steel has similar composition to 304L and is a common filler material for weldments between ferritic and austenitic steels [14]. Both 308L and 309L undergo rapid solidification during welding and a dual phase microstructure develops that consists of γ austenite and δ ferrite. The percentage and microstructure of precipitated δ ferrite in 308L groove filler is dependent on the elemental composition and the cooling trajectory, respectively [15].

The γ' phase is reported in both proton and neutron irradiated 300 series γ austenite stainless steels [16-18]. Ni_3Si γ' is a cubic crystal structure with a lattice parameter of 0.354 nm [19], similar to the lattice parameter (0.361 nm [20]) of γ austenite. Ni-Si clusters with similar Ni-Si atomic ratio to γ' have been reported in neutron and ion irradiated 300 series γ austenite stainless steels as well

[21, 22]. Further, G-phase precipitation and spinodal decomposition have been observed in δ ferrite after neutron irradiation and proton irradiation [9, 23, 24]. Investigations of irradiation-induced damage have been performed on γ austenite [16, 21, 25]. Microstructural evolution of proton irradiated dual or mixed phase 308L filler has been reported as well [12, 26].

In this work, dual phase 308L weld joint material was irradiated with 2 MeV protons at 360 °C to a damage level of approximately 3 dpa at a depth of 10 μm and an overall range of approximately 20 μm. The goal of this work is to fill data gaps related to radiation-induced microstructure of dual phase 308L, complementing our previous work [8, 9]. We also present evidence of scaling of void and G phase particle density with the differential energy to recoils associated with proton irradiation. Atom probe tomography (APT), high-resolution scanning transmission microscopy (HR-STEM), and energy dispersive spectroscopy (STEM-EDS) were performed on adjacent γ austenite and δ ferrite grains after proton irradiation to provide an understanding of the precipitation, void formation, and clustering processes in both phases. APT analysis provides insights into the local chemistry associated with phase boundaries, G phase particles, and Ni-Si cluster morphology. Further, we employ nearest neighbor analysis of the APT data set to determine ensemble-averaged feature specific composition profiles. Finally, we demonstrate a dependence of the irradiation induced changes to dpa, the latter varying greatly with depth.

2. Experimental procedures

2.1 Materials

The composition of the SA508-304L DMW starting materials used in this work are listed in Table 1. This weldment was fabricated at the Electric Power Research Institute (EPRI) using the gas tungsten arc welding (GTAW) technique [8, 9]. 309L butter was applied to the SA508 and

post-weld heat treatment (PWHT) was then performed at 635 °C ± 10 °C for 1.5 hours to relieve residual stress. The temperature ramp rate of heating and cooling were below 70 °C/h when the temperature was above 220 °C. The width of 309L butter was approximately 15.6 mm. 309L butter was welded to the 304L using 308L filler with bevel angle of 60 degrees. Both the 309L butter and 308L filler material recrystallizes upon cooling into a mixed phase microstructure of δ ferrite and γ austenite. A single γ austenite phase dilution zone forms between the SA508 and 309L that we have analyzed previously [8].

Table 1. Composition of the SA508-304L DMW starting materials.

Materials (at.%)	Cr	Ni	Mn	Mo	C	Cu	N	P	Si	Fe
SA508	0.18	0.76	1.38	0.47	1.01	0.08	NA	0.02	0.45	95.64
309L	24.38	12.80	1.60	0.04	0.05	0.09	NA	0.04	0.93	60.08
308L	21.07	9.69	1.99	0.09	0.07	0.24	NA	0.04	1.02	65.78
304L	19.23	7.53	1.73	0.19	0.09	0.38	0.27	0.05	0.55	69.96

2.2 Experiments and Analytical Techniques

Tensile specimens and transmission electron microscopy bars were irradiated with protons at the Michigan Ion Beam Laboratory (MIBL). These samples were cut from 308L filler and mechanically polished using SiC grit paper. Residual surface damage was removed by electropolishing with a 90-10 methanol-perchloric electrolytic solution at -30 °C. A potential of 40 V was applied between the electrolyte and the 308L specimen for 15 s.

A 3 MV National Electronics Corporation Pelletron accelerator in the MIBL was used to generate 2 MeV protons to irradiate the 308L samples. Proton irradiation was performed at 360 °C under a base pressure of 10^{-7} Torr. The total proton current was 30 micro-Amps over a 1.12 cm^2 area. The total irradiation time was 140 hours. The irradiation temperature was set to compensate dose rate difference between neutron (approximately 300 °C in LWRs) and proton

irradiation according to invariance theory of Mansur [27]. Simulated damage profiles of the irradiations were calculated by Stopping and Range of Ions in Matter (SRIM) [28], as shown in Figure 1. Two-MeV protons have a damage profile with a maximum at about 18 µm in 308L. The calculated damage level of 3 dpa is achieved at a ~10 µm depth of 60% of the Bragg peak (the peak in Figure 1) in a 140 h irradiation test, corresponding to a damage rate of 10^{-5} dpa/s. The estimated dpa at 60% of the Bragg peak (2 MeV protons have a range of ~18 µm in 300 series austenitic steel [21]) is 3 dpa using a calculated damage energy of 2.8 keV following the procedure recommended by Stoller *et al*. [22]. The use of 2 MeV protons to this value of dpa is typical for proton irradiated steels used by others [16, 25] and represents an approximate saturating damage level with respect to radiation induced segregation.

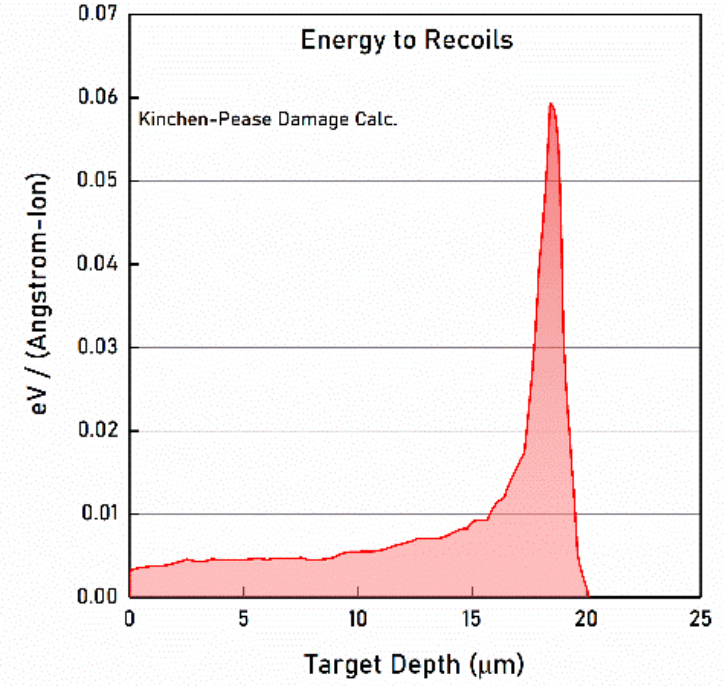

Figure 1. Proton irradiation damage profile (differential energy to recoils) versus depth (zero is the free surface) in 308L simulated by SRIM for a 2 MeV incident proton energy.

A FEI Scios2 Dual-Beam SEM/FIB was used to acquire SEM images and to prepare lift-out specimens for TEM/STEM analysis. 10 µm by 10 µm and 10 µm by 20 µm lift out specimens were thinned with a Ga ion milling to less than 100 nm. A Pt layer was used to prevent ion beam damage to the analysis volume of the lift out.

STEM-EDS measurements were performed on FEI Scios2 FIB lift out TEM specimens with FEI Themis Z Advanced Probe Aberration Corrected Analytical TEM/STEM with a 4-crystal EDS detection system. A FEI Themis Z Advanced Probe Aberration Corrected Analytical TEM/STEM was used for obtaining high-angle annular dark-field (HAADF) and atomic resolution STEM micrographs as well.

Three-dimensional chemical composition data was collected from a needle-shaped tip specimen with a Cameca Local Electrode Atom Probe (LEAP) 5000XS. Several APT tips fabricated at the free surface were analyzed, but we present analysis of one tip that contained a γ–δ phase boundary and both G phase particles and Ni-Si clusters. The atom probe tomography (APT) specimen was fabricated using the FEI Scios2 Dual-Beam FIB/SEM. The APT tip specimen was approximately 80 nm base diameter and 350 nm length, and a total of 84 million atoms were collected for the APT analysis.

3. Results and Analysis

3.1 STEM analysis of G phase ($Mn_6Ni_{16}Si_7$) precipitates and Ni-Si enriched clusters

3.1.1 G phase ($Mn_6Ni_{16}Si_7$) and Ni-Si clusters

Figure 2a is a high-angle annular dark-field (HAADF) micrograph of proton irradiated δ ferrite and γ austenite in 308L. The STEM HAADF image was taken at an approximate depth of 10 μm below the free surface. Left side of the micrograph is a δ ferrite grain and the right side is a γ austenite grain. STEM-HAADF images show Z contrast (larger atomic number elements give greater/brighter contrast) as well as diffraction contrast. The Z contrast between δ ferrite and γ austenite is similar and the diffraction leads to the contrast observed in Figure 2a. Figures 2b-f are the STEM-EDS maps showing the distribution of elements in the region shown in Figure 2a. Ni-Si-Mn enriched precipitates are observed in the proton irradiated δ ferrite, as shown in Figures 2d-f. These Ni-Si-Mn enriched particles were confirmed as the G phase in our previous study using TEM diffraction and advanced computations [9]. In addition, Figures 2d-f also reveal Ni-Si enriched clusters which are depleted in Mn in the proton irradiated γ austenite. We referred to these as "Ni-Si enriched clusters" as opposed to second phase precipitates because our previous study demonstrated that unique diffraction reflections from these clusters were absent [9]. Ni-Si clusters in proton irradiated γ austenite have been reported by other researchers [16, 25]. Both G phase precipitates and Ni-Si enriched clusters in Figure 2 are poor in Fe and Cr. G phase particles in the proton irradiated δ ferrite have a cuboid shape with a diameter of approximately 20 nm. On the other hand, the Ni-Si enriched clusters in the proton irradiated γ austenite do not have a well-defined size and shape and, as Figure 2d indicates, these clusters have a line- and loop-like morphology.

A G phase particle and a Ni-Si cluster are marked by a yellow and red circle, respectively, in Figure 3a (the same HAADF image shown in Figure 2a). Figure 3b is a high-resolution (HR-) STEM micrograph of G phase precipitate in Figure 3a. A well-defined G phase lattice is observed in the host δ ferrite matrix; we previously confirmed the $[001]_G//[001]_\delta$ orientation relationship with a 45 degree rotation about this axis and a 4:1 lattice parameter ratio [9]. In contrast, the HR-STEM micrograph shown in Figure 3c of Ni-Si clustering indicates these features are coherent with the γ austenite matrix and phase separation has not occurred, consistent with the lack of additional diffraction reflections from these regions.

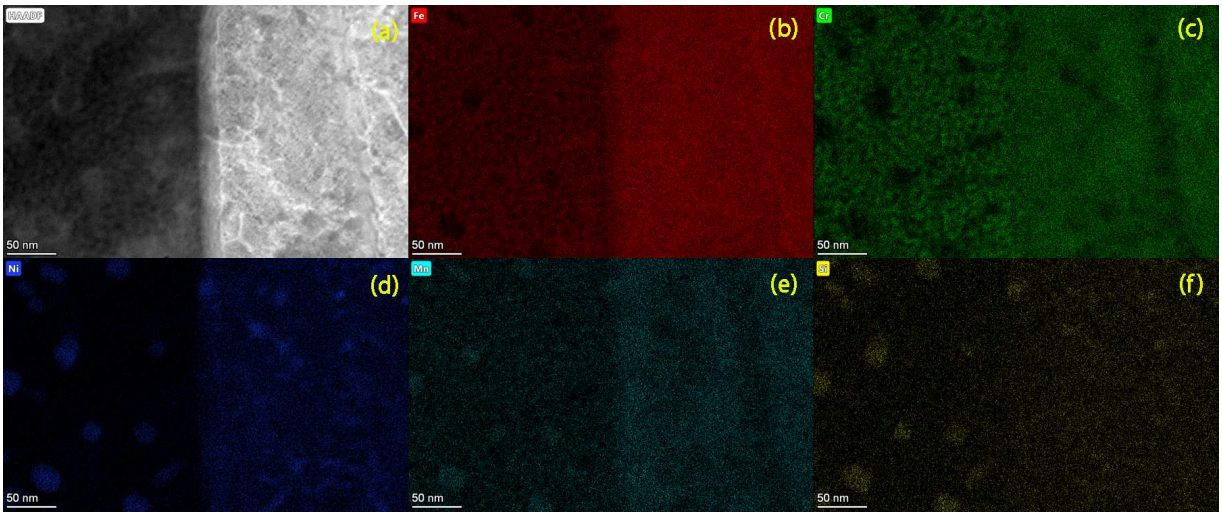

Figure 2. (a) HAADF image of phase boundary in proton irradiated 308L with a δ ferrite region (left) and a γ austenite region (right) at an approximate depth of 10 μm beneath the free surface, (b) STEM-EDS Fe map, (c) STEM-EDS Cr map, (d) STEM-EDS Ni map, (e) STEM-EDS Mn map, (f) STEM-EDS Si map. The scale bar in each figure is 50 nm.

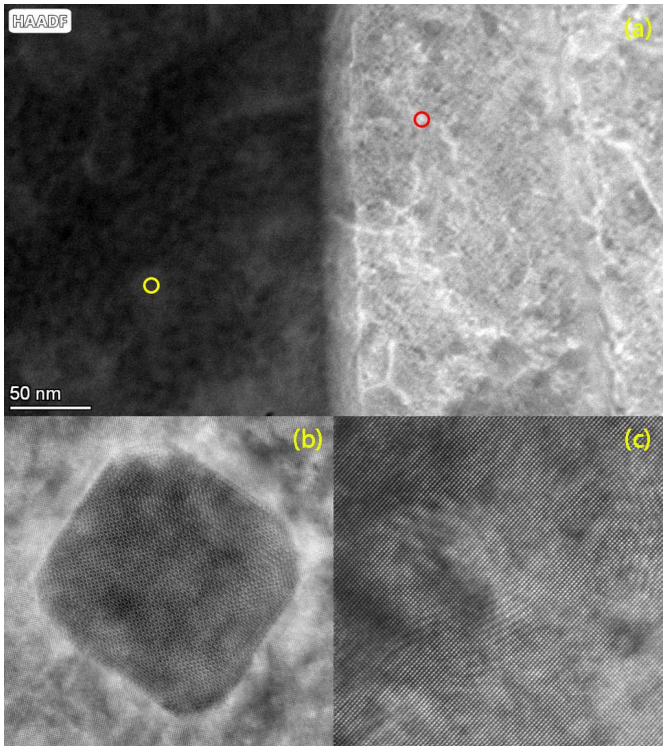

Figure 3. (a) HAADF image of proton irradiated δ ferrite (left) and γ austenite grain (right) at an approximate depth of 10 μm beneath the free surface; G phase particle is identified with a yellow circle and a Ni-Si enriched cluster is identified with a red circle, (b) HR-STEM micrograph of G phase from the yellow circle, (c) HR-STEM micrograph of Ni-Si enriched cluster from the red. The zone axis for Figures 3b and 3c is the [001]. The magnification of (b) and (c) are identical and represent a 15 by 15 nm^2 area.

Our previous study found that Ni-Si enriched clusters were commonly seen at the edge of voids in the proton irradiated γ austenite grains [9]. An atomic resolution HR-STEM micrograph of crystal structure near the edge of proton irradiation induced void is shown in Figure 4. This micrograph indicates that the lattice structure associated with Ni-Si clustering at the edge of the void is coherent with the host γ austenite matrix; in other words, phase separation did not occur at the edges of voids. Dark Z contrast is expected for voids since no elements are present. The interference patterns in Figure 3c and 4 are Moire fringes from overlapping of grains.

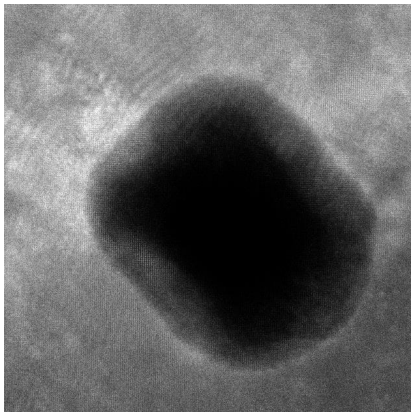

Figure 4. HR-STEM micrograph near the edge of a void in a proton irradiated γ austenite grain around 10 μm beneath the free surface. The zone axis is [001]. The magnification of the micrograph is the same as that for Figure 3b.

3.1.2 Elemental line-scan profiles of G phase, Ni-Si cluster and phase boundary with STEM-EDS data

Elemental line scans have been performed on a G phase ($Mn_6Ni_{16}Si_7$) precipitate in proton irradiated δ ferrite, at the phase boundary between a proton irradiated δ ferrite grain and a γ austenite grain, and for a Ni-Si cluster in a proton irradiated γ austenite grain. These line scans are shown in Figure 5. Figure 5b indicates that the G phase has Ni concentration of approximately 35 at. % and Si and Mn concentration of approximately 15 at. %. However, approximately 30 at. % of Fe and 15 at. % of Cr are detected in the G phase. Since diameter of G phase is approximately 20 nm, the Fe and Cr signals likely come from δ ferrite. Approximately 30 at. % Cr and 5 at. % Ni are detected in the proton irradiated δ ferrite in Figure 5c, which agrees with the Cr and Ni composition in irradiated δ ferrite matrix in Figure 5b. In addition, approximately 20 at. % Cr and 10 at. % Ni are seen in proton irradiated γ austenite in Figure 5c, which agrees with the Cr and Ni content in irradiated γ austenite in Figure 5d. The elemental line scan profile of the Ni-Si cluster in Figure 5d demonstrates that Ni is enriched. Si enrichment is clear in Figure 2f. Ni and Si enrichment is consistent with clustering of these elements. No evidence of Mn in the Ni-Si clusters

is seen in Figure 5d. Cr is depleted in the Ni-Si cluster, while no significant change of the Fe concentration. The EDS line scan of the δ–γ phase boundary (Figure 5c) indicates possible Cr enrichment. However, we do not believe this is statistically relevant given the scattering in the data and APT analysis of the same phase boundary presented below.

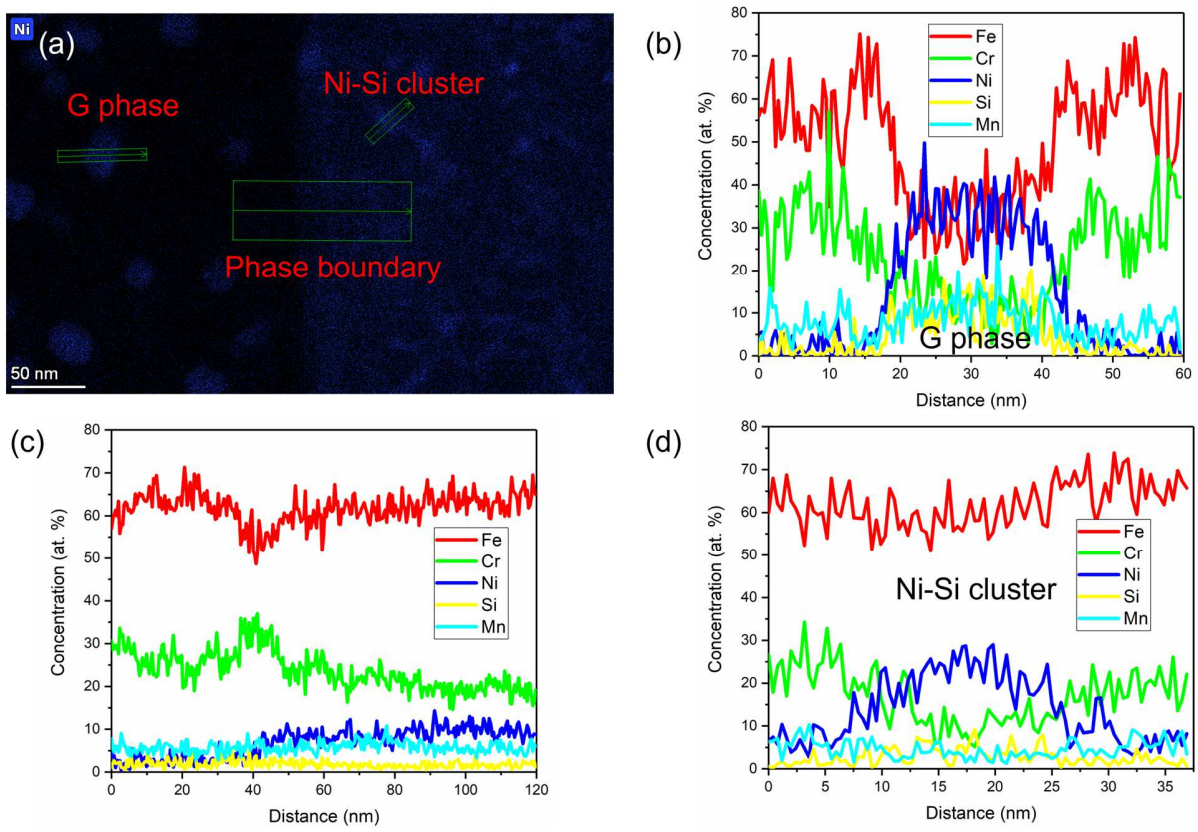

Figure 5. (a) STEM-EDS Ni map showing where the line scans are located, (b) elemental line scan profile of G phase ($Mn_6Ni_{16}Si_7$) in proton irradiated δ ferrite grain, (c) elemental line scan profile of δ-γ grain boundary, (d) elemental line scan profile of Ni-Si cluster in proton irradiated γ austenite grain. The width of the scanning line on G phase and Ni-Si cluster is 15 nm and that on the grain boundary of δ ferrite grain and γ austenite grain is 50 nm.

3.2 APT results for G phase precipitation and Ni-Si clustering in proton irradiated 308L

Iso-concentration surfaces (isosurfaces) from APT analysis at an atomic percent concentration of Ni-Si-Mn 15-6.6-5.6 , which corresponds to the atomic ratio of Ni, Si and Mn in the G phase, are shown in Figure 6. This rendering reveals the G phase particles and the Ni-Si clusters in the proton irradiated δ ferrite grain and γ austenite grain, respectively, at the free surface (recall the specimen was fabricated at the free surface). The G phase precipitates in δ ferrite have a spherical or cuboid morphology with a characteristic length of approximately 6 nm. According to the HR-STEM micrograph in Figure 3b (at a depth of 10 µm), the diameter of G phase particle is approximately 20 nm, indicating that the size of G phase precipitates increase with depth. We correlate the depth dependence of G phase particle density to displacement cascade damage below. As shown in Figure 6, Ni and Si segregate at the δ/γ phase boundary. In addition, Ni-Si enriched clusters with line and loop morphologies are observed in irradiated γ austenite. These features were detected with STEM-EDS in Figure 2d (Ni map), but the APT reconstructed renders these features in three-dimensions. Lin *et al*. believes the loop like features are formed due to Ni-Si enrichment along the boundary of Frank loops [12] and this would be consistent with our APT observations.

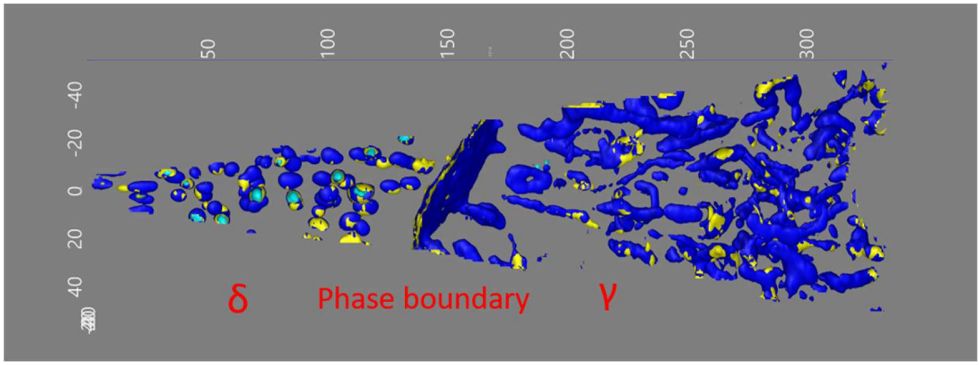

Figure 6. Ni, Si and Mn isosurfaces in an APT reconstructed tip. The reconstructed tip was fabricated from a FIB lift out at the free surface. The total length of the tip was approximately 350 nm. 15 at. % Ni (blue), 6.6 at. % Si (yellow) and 5.6 at. % Mn (cyan) isosurfaces were selected to reveal the G phase particles and Ni-Si enriched clusters in proton irradiated δ ferrite and γ, respectively. This specimen included a phase boundary near the middle of the tip. Approximately 84 million atoms were detected for this specimen.

Atom probe tomography facilitates analysis unique to this characterization technique. Here we use cylinders with diameter of 2 nm (smaller than the dimension of G phase particles and Ni-Si clusters) analyze the concentration profiles associated with the isosurfaces of the G phase, the δ-γ phase boundary, and the Ni-Si clusters. This analysis is shown in Figure 7. Elemental line-scan profiles (determined by averaging within the analysis cylinder) between G phase and bulk δ ferrite demonstrates that significant elemental variation is exists in two different phases, as indicated in Figure 7b. As expected, the G phase is rich in Ni, Si and Mn. Fe concentration changes from 65 at. % in δ ferrite to as low as 10 at. % in G phase. Cr decreases from 30 at. % in δ ferrite to 5 at. %. The Ni concentration is as high as 55 at. % in the G phase, while on 5 at. % in δ ferrite. In addition, Si and Mn concentration in the G phase are as high as 25 at. % and 15 at. %, respectively. In contrast, the variation of elements between Ni-Si cluster and γ austenite in Figure 7d is significantly smaller, as shown in Figure 7d. Ni and Si enrichment is observed in the Ni-Si clusters (spots 1 and 2 in Figure 7a), while Mn is not enriched at either location. Fe and Cr concentration differences between Ni-Si clusters and γ austenite are lower compared to those between G phase and δ ferrite. Ni concentration in Ni-Si clusters is as high as 35 at. % and Si concentration in spots 1 and 2 reached 10 at. %. Fe concentration changed from 65 at. % in γ austenite to 55 at. % in Ni-Si cluster, Cr from 20 at. % in γ austenite to 10 at. %. δ-γ phase boundary in Figure 7c is approximately 4 nm thick based on the segregation profiles. Cr is depleted within the phase boundary, while Ni and Fe are enhanced. These phase boundary composition changes are consistent with radiation-induced segregation, similar to that occurring at γ–γ grain boundaries in γ austenite [9]. Cr depletion at δ-γ phase boundaries has been observed by others as well [22, 26]. We noted above subtle Cr enrichment in Figure 5c at the δ-γ phase boundary. However, we do

not believe this feature is representative and likely due to the statistical nature of performing the line scan of STEM-EDS data, as discussed above.

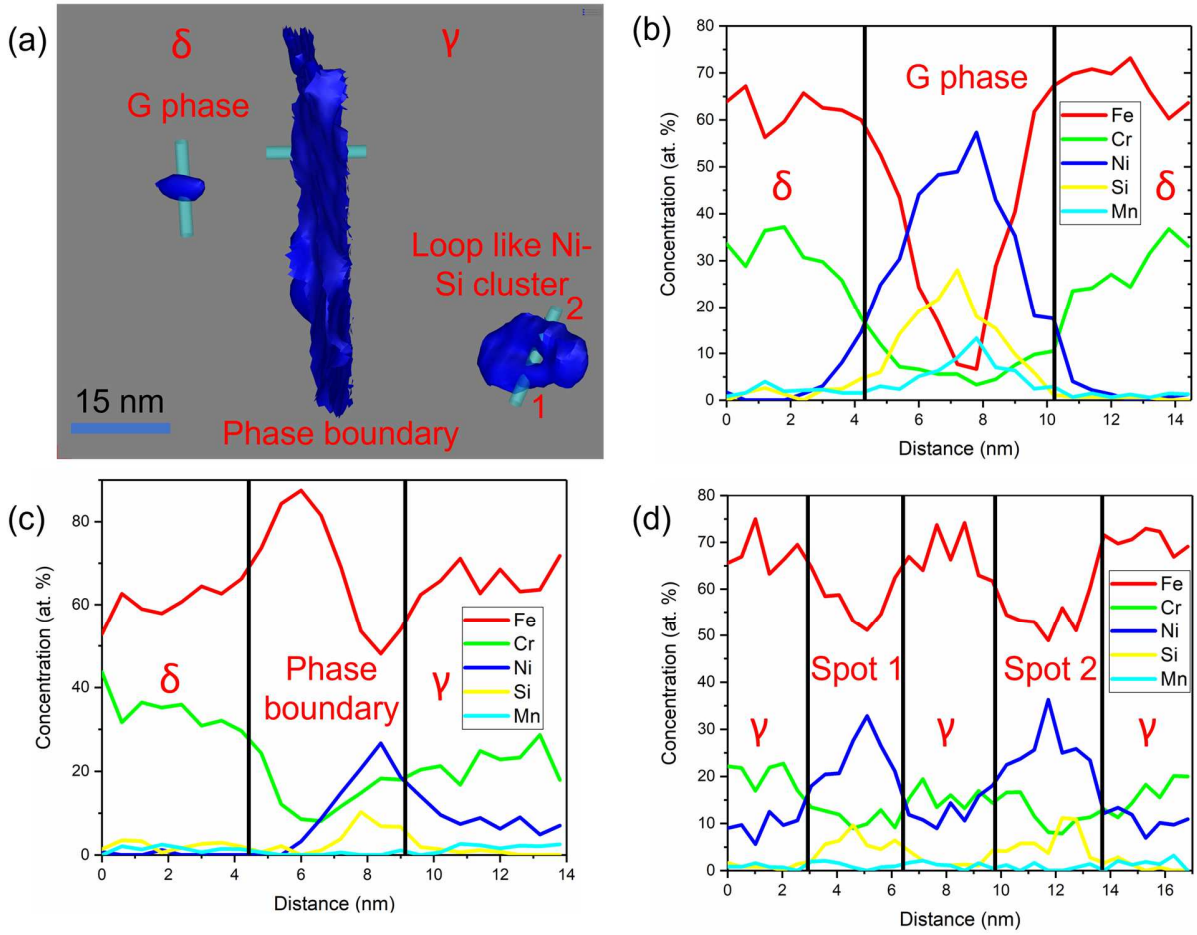

Figure 7. (a) 15 at. % Ni iso-concentration surfaces showing the location of analysis cylinders with diameter of 2 nm for a G phase in proton irradiated δ ferrite grain, a δ-γ grain boundary between proton irradiated δ ferrite and γ austenite grains, and a loop-like Ni-Si cluster; (b) elemental line scan profile of G phase ($Mn_6Ni_{16}Si_7$) in proton irradiated δ ferrite grain; (c) elemental line scan profile of δ-γ grain boundary; and (d) elemental line scan profile of Ni-Si cluster in proton irradiated γ austenite grain.

We further analyze the APT data set following a procedure similar to that used by Chen *et al*. [29]. These authors studied proton irradiated 304 stainless steel with APT and observed solute clustering and segregation at dislocations. Here we use nearest neighbor analysis to analyze G phase particles in δ ferrite and Ni-Si clusters in γ austenite in proton irradiated 308L. Parameters used for this

analysis are given in Table 2. The high order nearest neighbor (NN) distributions [29, 30] are used to determine D_{max}. D_{max} is defined as the maximum distance between two atoms that can be attributed to the same morphological feature such as a single G phase precipitate or a single Ni-Si cluster. As shown in Figure 8(a) and 8(c), the NN distributions associated with G phase particles and Ni-Si clusters separate with increasing order. The optimum order number is subjectively determined from Figures 8a and 8c where the peaks associated with G phase particles and Ni-Si clusters are sufficiently distinguishable. The 6^{th} and 5^{th} order plots (Figure 8(b) and 8(d)) were chosen for determining D_{max} for G phase particle and Ni-Si clusters, respectively. As shown Figure 8(b) and 8(d), D_{max} is set to cross over distance between the two Gaussian distributions used in the fitting of the NN distribution for G phase particles and Ni-Si clusters. Silicon was chosen for the nearest neighbor analysis because Si is in both morphological features.

All atoms within a distance of L (the envelop parameter) of a cluster/particle atom will be added to that cluster or particle. Features with an atom count under 100 (N_{min}) are not included in either the G phase particle or Ni-Si clusters distributions. In addition, $D_{errosion}$ is used to remove atoms from the edge of Ni-Si clusters. L and $D_{errosion}$ are related to chemical composition of segregated atom (Si) in G phase particles and Ni-Si clusters, L is chosen to be ¾ of D_{max} and $D_{errosion}$ to be ¼ of D_{max}. These parameters are listed in Table 2. Using these parameters, nearest neighbor analysis was performed in the δ ferrite and γ austenite regions of the APT tip; 62 G phase particles and 86 Ni-Si clusters were selected.

Table 2. Parameters for Nearest Neighbor Analysis based on Si in APT tip.

	Order	D_{max} (nm)	N_{min}	L (nm)	$D_{erosion}$ (nm)
δ ferrite	6	0.65	100	0.49	0.16
γ austenite	5	0.75	100	0.56	0.19

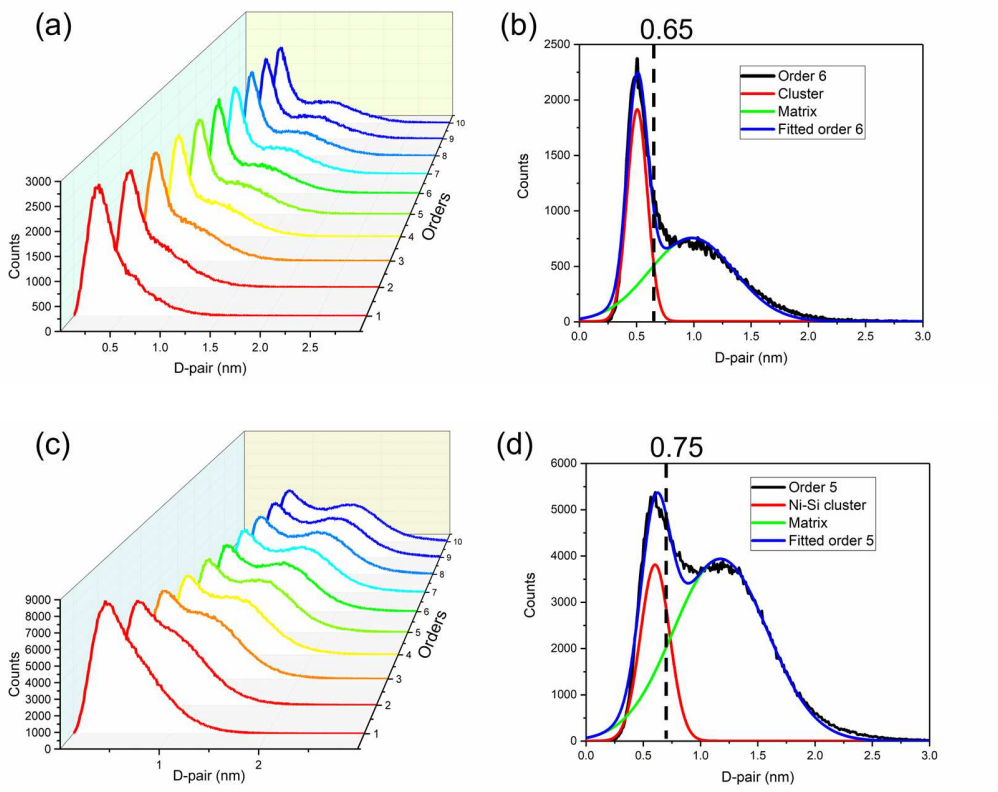

Figure 8. (a) Si-Si nearest neighbor distributions in δ ferrite for orders from 1 to 10; (b) the Gaussian peak deconvolution for the Si–Si nearest neighbor distribution with an order of 6; (c) Si-Si nearest neighbor distributions in δ ferrite for orders from 1 to 10; (d) the Gaussian peak deconvolution for the Si–Si nearest neighbor distribution with an order of 5.

The utility of nearest neighbor analysis is that a normalized composition profile can be determined for all selected Ni-Si clusters and G phase particles. This analysis is shown in Figure 9. The composition profile of the 62 G phase particles and 86 Ni-Si clusters are plotted in these normalized concentration profiles. The boundary between the morphological feature and the host matrix is placed at a normalized distance of one. The normalized concentration profiles agree well with the APT line scans in Figure 7. In general, Ni, Cr, and Fe concentration gradients are smaller for the Ni-Si clusters. This is consistent with the lack of second phase precipitation associated

with Ni-Si clusters. On the other hand, TEM evidence in our previous work [9] indicates that the G phase particles are a distinct second phase and sharper concentration gradients are expected.

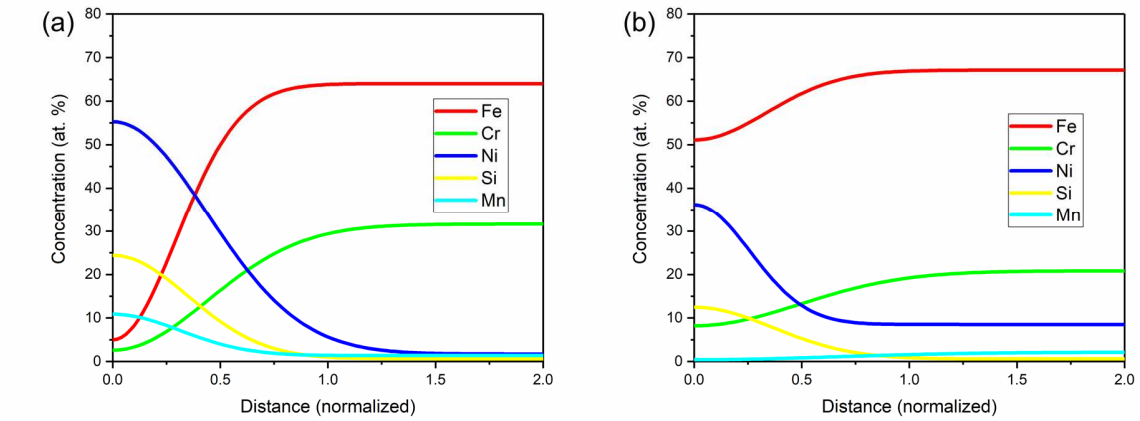

Figure 9. (a) Normalized concentration profile between G phase particles and δ ferrite and (b) normalized concentration profile between Ni-Si clusters and γ austenite.

3.3 Analysis of proton irradiation induced voids in γ austenite

In addition to G phase precipitates and Ni-Si clusters our previous study included evidence of void formation in the proton irradiated γ austenite [9]. STEM images of voids at 12, 16, and 18 μm below the free surface are shown in Figure 10. Density of these voids versus depth is calculated from number of voids in a 575 nm by 575 nm STEM micrograph cross section with the thickness determined by EELS analysis. The thicknesses determined with EELS at depths of 12, 16, and 18 μm are 246, 190, and 152 nm, respectively, using an inelastic mean free path of 114 nm for 308 γ austenite [31]. Using these thickness values and the STEM micrograph void count (46, 90, and 130 voids were identified in Figure 10c, 10b and 10a, respectively), the corresponding void densities are 0.6×10^{21}, 1.4×10^{21}, 2.6×10^{21} m^{-3} at depths of 12, 16, and 18 μm, respectively. We plot these values together with G phase precipitate density in δ ferrite below.

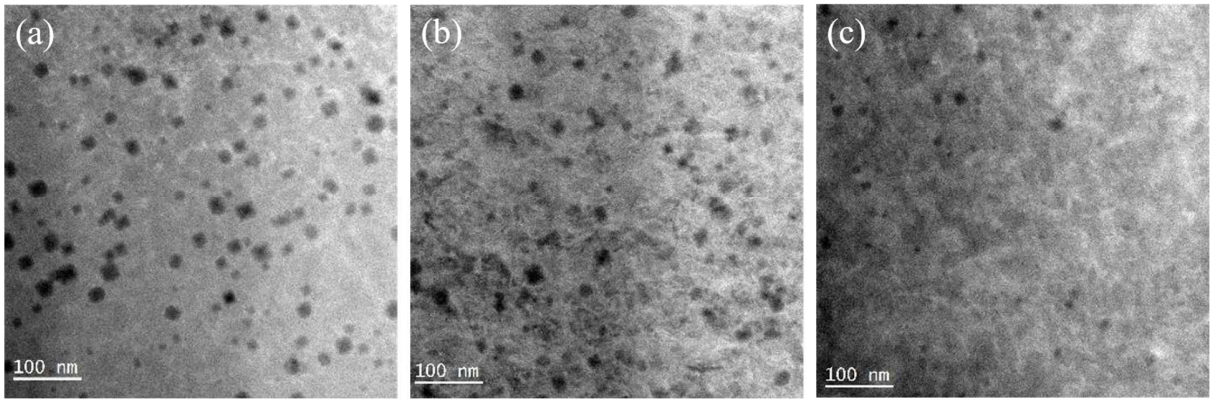

Figure 10. STEM micrographs of proton irradiation induced voids in γ austenite at depths of (a) 18 (b) 16 µm, and (c) 12 µm.

3.4 Bulk compositional analysis of proton irradiated 308L with STEM-EDS and APT

Table 3 presents the compositions of proton irradiated δ ferrite and γ austenite determined from STEM-EDS and APT analyses. The compositions of δ ferrite and γ austenite are obtained from a 200 nm by 150 nm and 200 nm by 150 nm areas, respectively, in Figure 3a. The composition analysis from the APT rendering of δ ferrite uses a cylinder with a diameter 100 nm and length of 150 nm and the δ ferrite grain in Figure 6. Composition analysis of γ austenite is performed using a larger cylinder with a diameter 200 nm and length 150 nm in the γ austenite grain in Figure 6. The composition of each phase from STEM and APT agree to within 1 atomic percent in Table 3.

Table 3. Composition of δ ferrite and γ austenite of irradiated 308L from STEM-EDS and APT.

Materials (at. %)	Cr	Fe	Ni	Si	Mn
δ ferrite (STEM-EDS)	31.0	62.6	3.1	1.5	1.8
δ ferrite (APT)	30.1	63.5	3.6	1.2	1.6
γ austenite (STEM-EDS)	20.9	66.6	8.9	1.0	2.6
γ austenite (APT)	20.4	67.7	9.0	0.9	2.0

The APT line-scan profiles in Figure 7b of the G phase show significant Fe and Cr concentration, implying that Fe and Cr replaces Mn in the G phase. These elements neighbor each other on the periodic table and have similar ionic radii. The stoichiometric formula of the G phase is $M_6Ni_{16}Si_7$,

where M is a transition metal [16]. The Si concentration from G phase in Figure 7b is as high as 25 at. %, while the maximum Mn concentration from G phase in Figure 7b is 15 at. %. The atomic ratio of Si to Mn in G phase is therefore 1.7, significantly higher than the stoichiometric atomic ratio of 1.17. Therefore, it is likely Fe and Cr substitute for Mn in the G phase lattice in our proton irradiated material.

Isosurfaces of the G phase precipitates are shown in Figure 11. The phase boundary and the Ni-Si clusters are rendered as well. Iron and Cr isosurface maps are shown in Figures 11d and clearly indicate that Fe and Cr are substitutional elements in the G phase precipitates. In addition, Figure 11f confirms that Mn is only observed in the G phase and not in Ni-Si clusters.

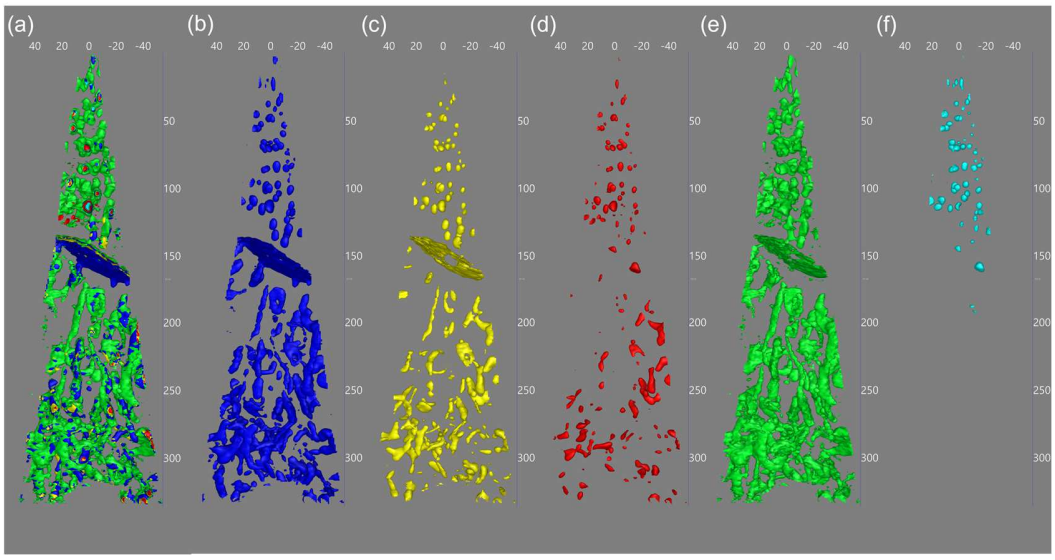

Figure 11. (a) Ni, Si, Fe, Cr and Mn isosurfaces of proton irradiated δ ferrite and γ austenite grain, (b) 28 at. % Ni isosurface in δ ferrite, 23 at. % Ni isosurface at the δ-γ grain boundary in γ austenite, (c) 10 at. % Si isosurface δ ferrite and 5 at. % Si isosurface at the δ-γ grain boundary and in γ austenite grain, (d) 38 at. % Fe isosurface δ ferrite and 55 at. % Fe isosurface at the δ-γ grain boundary and in γ austenite, (e) 17 at. % Cr isosurface δ ferrite and 15 at. % Cr isosurface at the δ-γ grain boundary and in γ austenite, (f) 5 at. % Mn isosurface δ ferrite grain and 5 at. % Mn isosurface at the δ-γ grain boundary and in γ grain.

3.5 Analysis of G phase Precipitation in Proton Irradiated δ Ferrite

Figure 1 demonstrates the differential energy to recoil atoms in 308L increases to a peak at a depth of approximately 18 μm. TEM specimens were lifted out at depths of approximately 10 and 18 μm. The APT specimen was taken from the free surface. The corresponding displacements per atom (dpa) increases from approximately 2 dpa at the free surface, to 3 dpa at 12 μm (this depth corresponds to 60% of the peak depth), to approximately 40 dpa at a depth of 18 μm corresponding to the peak in Figure 1. These dpa values were calculated using the NRT model with a 40 eV displacement energy and a zero eV lattice energy as described above.

We assume a spherical morphology for the G phase particles. The histogram plot in Figure 12d is generated after processing 59 G phase particles in a 50 nm by 150 nm APT Ni isosurface map (Figure 12a) with a Ni concentration of 28 at. %. In the previous section, APT nearest neighbor analysis found 62 G phase particles in proton irradiated δ ferrite, which agrees well with 59 G phase particles found from this APT isosurface rendering. In addition, the largest diameter at the tip-end of δ ferrite grain, seen in Figure 12a, is less than 50 nm, which is two times smaller than our TEM sample (approximately 100 nm). Over 70 % of the G phase particles have the diameter between 3 to 6 nm in Figure 12d. After analyzing a total of 49 G phase particles in a 500 nm by 500 nm TEM bright field micrograph (Figure 12b) captured at a depth of 10 μm, histogram in Figure 12e indicates that 60 % of the 49 G phase particles have the diameter ranging from 15 nm to 30 nm. In addition, histogram in Figure 12f is produced after processing 72 G phase particles in a 300 nm by 300 nm TEM bright field micrograph (Figure 12c). Around 80 % of the 72 G phase particles have the diameter in the range of 20 to 35 nm. A trend of increasing precipitate size with depth and ion damage is therefore deduced. The APT size distribution in Figure 12d is strongly influenced by the isosurface concentration, 28% at. Ni in this case. The isosurface

concentration associated with the G phase boundary can be estimated using Figure 11a. However, this is subjective; the Fe-Ni and Cr-Ni cross over distances, for example, correspond to 40 and 20 % at., respectively. The 28% at. Ni isosurface represents a compromise between these two cross over points. Still we could hypothesis that the APT G phase size distribution associated with an isosurface of 28% at. Ni underestimates the actual size distribution, but not by a factor greater than two (the factor corresponding to a normalized size of 1 in Figure 11a). The G phase particle size distribution at the free surface even with this hypothesis is smaller than those at 10 and 18 nm.

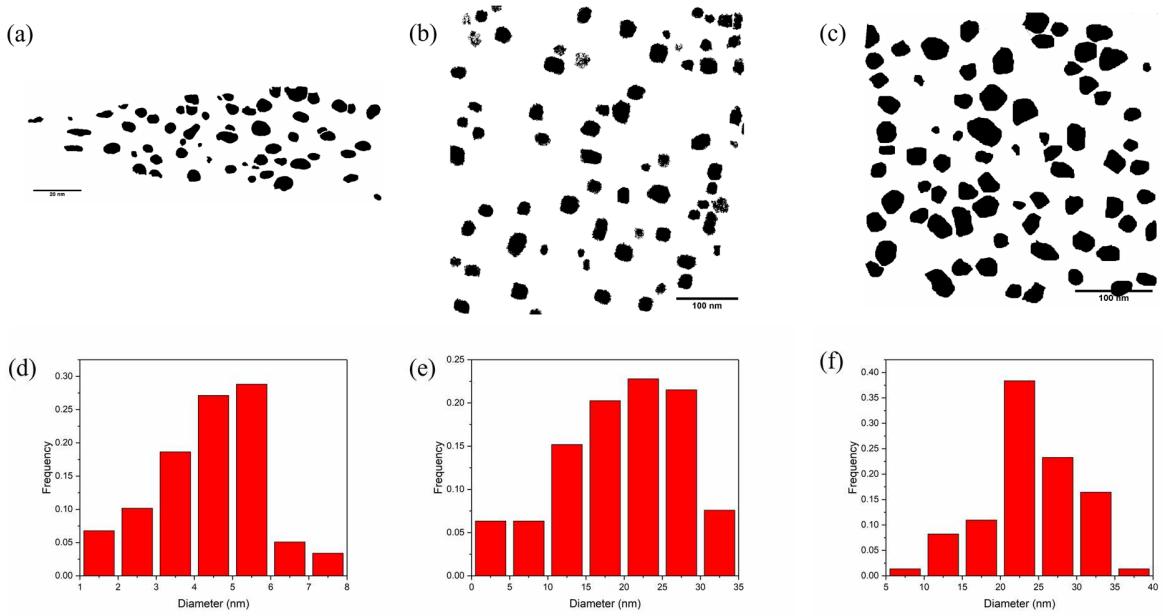

Figure 12. (a) Reconstructed APT image of G phase precipitates in proton irradiated δ ferrite at a depth of 100 nm processed by ImageJ, (b) TEM image of G phase precipitates in proton irradiated δ ferrite at a depth of 10 µm processed by ImageJ, (c) TEM image of G phase precipitates in proton irradiated δ ferrite at a depth of 18 µm processed by ImageJ, (d) Histogram of size distribution of G phases in proton irradiated δ ferrite grain from the reconstructed APT micrograph at 10 nm, (e) Histogram of size distribution of G phases in proton irradiated δ ferrite grain from the TEM micrograph at 10 µm, and (f) Histogram of size distribution of G phases in proton irradiated δ ferrite grain from the TEM micrograph at 18 µm.

Since the volume of the APT tip is known and the thickness of TEM specimens at 10 and 18 µm was measured with EELS, the G phase particle density at free surface and at depths of 10 and 18

μm are determined as 1.6×10^{23}, 0.2×10^{21}, and 5.3×10^{21} m^{-3}, respectively. These are listed in Table 4. The G phase particle density scales with the differential energy to recoils for 10 and 18 μm. Similar scaling is observed for the calculated G phase volume fraction. The ratio of the 18 to 10 μm G phase particle density and volume faction are 27 and 35 using the values from Table 4, respectively. This is reasonable agreement given the coarse fidelity of the G phase particle distributions. However, the G phase particle density and volume fraction at the free surface are disproportionally large. One possible explanation for this observation is that the large point defect flux to the free surface, which is an unbiased sink, facilitates nucleation and growth.

Table 4. G phase density and volume fraction at different depth in δ ferrite.

Depth (μm)	Density ($1/m^3$)	Volume Fraction
0.1	1.6×10^{23}	0.0093
10	0.2×10^{21}	0.0013
18	5.3×10^{21}	0.0452

We overlay the calculated G phase particle densities at 10 and 18 μm on the TRIM damage profile in Figure 13. The void densities determined with the Figure 12 data are also included in Figure 13. Overall, the G phase particle density, G phase volume fraction, and void density scale with differential damage at 10 and 18 μm, while the near-surface G phase particle density from analysis of the APT data does not scale with damage. We discuss this in the next section.

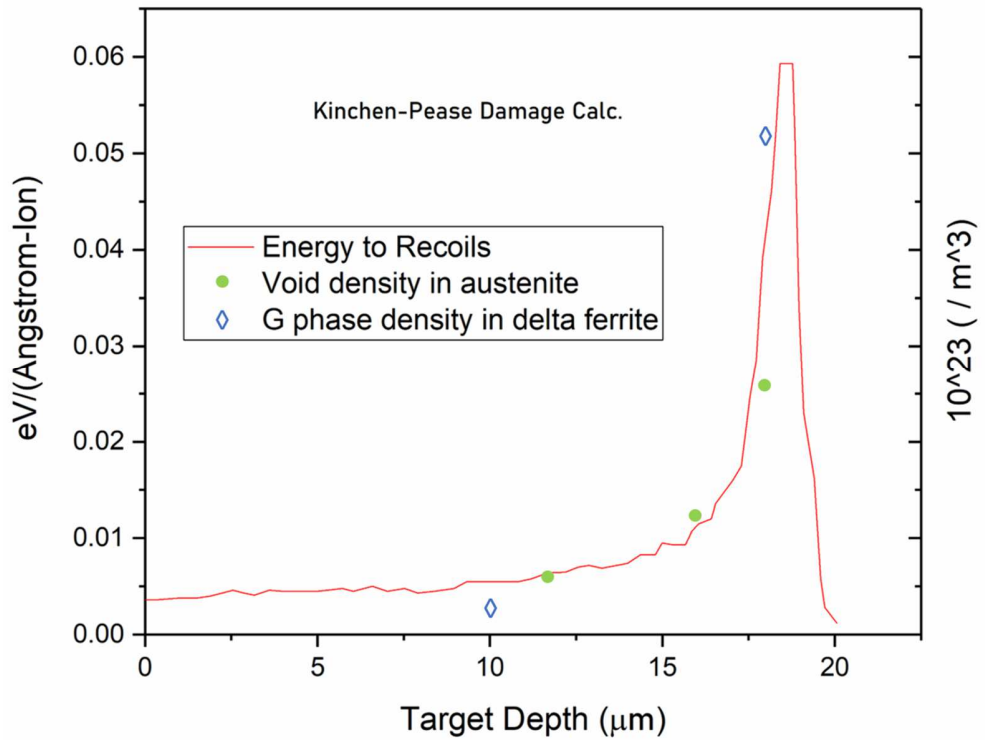

Figure 13. Void and G phase particle densities in proton irradiated γ austenite and δ ferrite as a function of depth overlaid with proton irradiation damage profile (differential energy to recoils) in 308L simulated by TRIM. The left-hand y axis is the damage profile and the right-hand y axis is the G phase and void particle density.

4. Discussion

The proton irradiated void density in γ austenite and G phase particle density in δ ferrite correlate to the proton irradiation damage profile, as seen in Figure 13. This is to be expected since the elevated point defect density associated with ion irradiation will facilitate the formation of both voids and G phase particles. The exception is the G phase particle density from APT analysis, which is thirty times higher at the free surface compared to the density at 18 μm (the approximate depth corresponding to the Bragg peak of the damage profile). The volume fractions are similar due to the small particle size distribution at the free surface. We mentioned above a possible explanation for the disproportionate free surface density above. A second possible explanation is that it is an artifact of the APT technique and associated analysis. The G phase particle density requires the tip volume and this volume relies upon accurate dimensions of the tip. We confirmed the tip dimensions by calculated the atomic number density from the known number of total atoms collected (84M) during APT analysis. This result is 8.5×10^{22} 1/cm^3, in good agreement with the average value of delta ferrite and gamma austenite. Thus we believe our tip dimensions are accurate to within 10%. The number of G phase particles in the δ ferrite portion of APT tip is maybe influenced by the isosurface concentration. We have investigated this effect and find the total number of G phase particles to be independent of the concentration chosen for the isosurface rendering. We therefore believe the near-surface G phase particle density to be real and not an artifact of APT analysis or rendering. We suspect it is due to the free surface acting as a point defect sink. This will elevate the point defect flux toward the surface and this elevated point defect flux may have induced greater precipitation. We also noted above that the G phase particle size distribution is finer for APT analysis at the free surface compared to STEM-EDS analysis at greater depths. The particle size distribution is certainly influenced by the isosurface rendering

concentration. Atom probe tomography also indicates Ni-Si clustering in γ austenite at the free surface (Figure 6) is at a finer scale than that observed at 10 μm (Figure 2d). This too could be related to elevated point defect fluxes. In the case of Ni-Si clusters, the rendering is very sensitive to concentrations selected for isosurface generation and comparing this morphology to TEM should keep this in mind. While we cannot offer proof that elevated point defect fluxes to the free surface caused these observations, it is plausible. Greater embrittlement would be associated with elevated G phase particle density near the free surface. Any process that is exacerbated by embrittlement near the free surface (IASCC, for example) could then be enhanced.

Others have observed Cr distributions in neutron irradiated cast 308L that are attributed to spinodal decomposition [23]. We also observe similar Cr morphologies in our APT renderings (the upper region Figure 11e) of proton irradiated δ ferrite 308L. And while we have no proof our Cr morphology is due to spinodal decomposition, the similarity with the Li *et al*. measurements suggests this may be the case. This becomes an interesting observation since an important difference between our work and that of Li *et al*. exists; ion versus neutron irradiation, respectively, and the associated significant difference in dose rate and total dose (both of which were very low for the neutron irradiated samples of Li *et al*. [23]).

The lattice parameter (1.112 nm) of $Mn_6Ni_{16}Si_7$ [32] is close to 4 times of δ ferrite (0.290 nm) [33], which leads to a reduced volumetric strain energy while $Mn_6Ni_{16}Si_7$ precipitating in δ ferrite. Our recent first-principles simulation suggested that G phase precipitation in δ ferrite requires much lower energy than in γ austenite, largely due electron/magnetic factors [9].

The Ni-Si clusters we observe in γ austenite may be precursors to Ni_3Si γ' formation that is known to occur in irradiated austenitic steels [17, 18]. The lattice parameter (0.361 nm [20]) of γ austenite

is close to that of γ' Ni_3Si (0.354 nm) and misfit strain will be low. On the other hand, misfit lattice strain of γ' Ni_3Si in δ ferrite (0.290 nm) will be large. Unlike the G phase precipitates in proton irradiated δ ferrite, Ni-Si clusters in irradiated γ austenite are depleted in Mn and Cr but not in Fe (Figure 2). In other words, the Ni-Si cluster composition is similar to the γ austenite matrix and accordingly the lattice structure of Ni-Si clusters shown in Figures 3c and 4 is commensurate with the γ austenite matrix. It is logical then to hypothesize that the Ni-Si clusters in irradiated γ austenite are precursors, presumably needed greater ion damage at temperature to precipitate into γ' Ni_3Si particles.

Elemental depletion and segregation at crystal defects such as dislocation loops, voids, and grain boundaries in irradiated γ austenite has been observed by us and others [9, 12, 16, 25]. The APT rendering shown in Figure 6 and associated composition is consistent with G phase particle formation in proton irradiated δ ferrite, which we see under STEM-EDS (Figure 2) and HR-STEM (Figure 3). In addition, Ni-Si clusters are observed in proton irradiated γ austenite in Figure 6. Some of the Ni-Si clusters have loop-like shape, which likely is due to Ni and Si segregation on dislocation loops [12, 16]. Although both dislocation loops [25] and voids [9] can be observed with TEM and HR-STEM images, Ni-Si clusters do not result in diffraction contrast [9]. This demonstrates that these clusters are not a second phase, but rather regions of elemental segregation that are commensurate with the host γ austenite lattice.

Composition profiles for the G phase particles, the Ni-Si clusters, and the δ–γ phase boundary are shown in Figure 7. Ni, Si, and Mn are the major elements in the G phase and the concentration of these elements is elevated above the δ matrix (Figure 7b). Much less concentration difference is observed between circular Ni-Si enriched clusters and γ austenite (Figure 7d). We note the ratio of Ni to Si in these clusters is approximately 3 to 1, which is the ratio in γ' Ni_3Si. The δ–γ phase

boundary concentration profile (Figure 7c) exhibits slight segregation of Ni and Si and depletion of Cr. We noted in our previous study that Cr is depleted and Ni and Si are enriched at γ–γ grain boundaries. Cr depletion at γ–γ grain boundaries is thought to be an influencing factor in irradiation-assisted stress corrosion cracking [34, 35].

5. Conclusions

1. The morphology of Ni-Si clusters and the size distribution and density of G phase precipitates and voids have been characterized in proton irradiated 308L, a weldment filler material with a dual δ–γ phase microstructure, with STEM-EDS and APT. These results corroborate previous work by us of precipitation and clustering induced by ion irradiation of dual phase weldment 308L groove filler material and extends the analysis to include the depth dependence of G phase particle density and void density. Scaling of both the void and G phase particle density to the differential proton damage profile is demonstrated.
2. APT nearest neighbor analysis was used to for G phase particles and Ni-Si clusters in δ ferrite and γ austenite, respectively. This analysis allowed the composition and composition gradients of the morphological features to be determined for an ensemble average collection. In addition, a γ–δ phase boundary was capture in the APT tip specimen. A line scan of across this phase boundary demonstrates Cr is depleted.
3. Analysis of the APT data for G phase particles shows a significant concentration of Fe and Cr in the $M_6Ni_{16}Si_7$ formula unit as the transition metal (M) substitutes. The observed Si to Mn atomic ratio (1.7) is significantly higher than that expected (1.2), indicating other transition metal elements must present to compensate for the observed of Si to M ratio.

The APT Fe and Cr isosurfaces created with median concentration between G phase and matrix δ ferrite gives direct evidence that both Fe and Cr are constituents.

4. APT renderings of Cr in proton irradiated δ ferrite in 308L suggest spinodal decomposition when compared to the work of others that show similar Cr elemental distributions in neutron irradiated cast 308L. This is another example of ion irradiation yielding similar microstructure characteristics as neutron irradiation even when the dose rate and total dose are greatly different.
5. G phase particle density in proton irradiated δ ferrite and void density in proton irradiated γ austenite agree well with the trend of proton irradiation differential energy to recoil profile as a function of depth. The exception is the G phase density at the free surface from APT analysis.
6. G phase particles near the free surface were analyzed with APT and the particle density and size distribution were determined. The density is significantly greater compared to those at greater depths. We suspect point defect fluxes to the free surface facilitate enhanced precipitation. The significantly larger G phase particle density at the free surface could have negative implications for processes that leverage embrittlement at the free surface (IASCC, for example).
7. Ni-Si enriched clusters were observed with STEM-EDS and APT in proton irradiated γ austenite. The Ni-Si clusters are commensurate with the host lattice in HR-STEM analysis, indicating the lack of second phase precipitation. These clusters are rich in Ni and Si but poor in Mn and the atomic ratio of Ni to Si is close to 3:1. We present APT analysis of these clusters at the free surface. This analysis indicates that Ni-Si clusters have a finer

size distribution compared to clusters at greater depths. Nearest-neighbor analysis yields an ensemble average composition profile for the Ni-Si clusters.

6. Acknowledgement

This work was supported by the US Department of Energy Nuclear Energy University Programs under contract number DE NE0008699. The Michigan Ion Beam Laboratory was used to perform the proton irradiation exposures. The authors are grateful to Drs. G. Was and O. Toader at the University of Michigan for performing the irradiations, as well as Dr. M. Song for help with sample electropolishing. A portion of the experiments were carried out at the Materials Research Laboratory Central Research Facilities, University of Illinois. The National Science Foundation under award number DMR 1828450 is gratefully acknowledged for the APT measurements. The authors are grateful to Dr. M. Sardela at the University of Illinois for a financial offset associated with APT data collection and analysis.

7. Contribution

Zhen Li: experimental analysis, methodology, interpretation, writing and editing-original draft preparation. Xun Zhan: HR-STEM and EELS, reviewing and editing. Waclaw Swiech: APT measurements and 3D reconstruction. Honghui Zhou, APT tip fabrication. Weicheng Zhong: sample preparation, reviewing, and editing. Carly J. Romnes: APT 3-D reconstruction and data analysis. Dhruval K. Patel: APT 3-D reconstruction and data analysis. Nachiket S. Shah: APT 3-D reconstruction and data analysis. Benjamin J. Sutton: weldment preparation. Brent J. Heuser: project direction, funding acquisition, supervision, conceptualization, writing, reviewing, and editing.

Reference

1. Seifert, H.P., et al., *Environmentally-assisted cracking behaviour in the transition region of an Alloy182/SA 508 Cl.2 dissimilar metal weld joint in simulated boiling water reactor normal water chemistry environment.* Journal of Nuclear Materials, 2008. **378**(2): p. 197-210.
2. Kim, S., et al., *Effects of alloying elements on mechanical and fracture properties of base metals and simulated heat-affected zones of SA 508 steels.* Metallurgical and Materials Transactions A, 2001. **32**(4): p. 903-911.
3. Ming, H., et al., *Microstructural characterization of an SA508–309L/308L–316L domestic dissimilar metal welded safe-end joint.* Materials characterization, 2014. **97**: p. 101-115.
4. Niu, W., et al., *Stress–Corrosion Cracking of Surface-Engineered Alloys in a Simulated Boiling-Water Reactor Environment.* Corrosion, 2018. **74**(6): p. 635-653.
5. Garcia, C., et al., *Stress corrosion cracking behavior of cold-worked and sensitized type 304 stainless steel using the slow strain rate test.* Corrosion, 2002. **58**(10): p. 849-857.
6. Andresen, P.L. and G.S. Was, *A historical perspective on understanding IASCC.* Journal of Nuclear Materials, 2019.
7. Song, M., et al., *Radiation damage and irradiation-assisted stress corrosion cracking of additively manufactured 316L stainless steels.* Journal of Nuclear Materials, 2019. **513**: p. 33-44.
8. Zhong, W., et al., *Residual stress, microstructure, and hardness of the dissimilar metal welds of SA508-309L-308L-304L.* Materials Science and Engineering: A, 2020.
9. Li, Z., et al., *Modified Microstructures in Proton Irradiated Dual Phase 308L Filler Material.* Journal of Nuclear Materials, 2021.
10. NRC, U., *Expanded Materials Degradation Assessment Volume 2: Aging of Core Internals and Piping Systems*. 2014, NUREG/CR-7153.
11. Dong, L., et al., *Microstructure and stress corrosion cracking of a SA508-309L/308L-316L dissimilar metal weld joint in primary pressurized water reactor environment.* Journal of Materials Science & Technology, 2020. **40**: p. 1-14.
12. Lin, X., et al., *Corrosion of phase and phase boundary in proton-irradiated 308L stainless steel weld metal in simulated PWR primary water.* Corrosion Science, 2020. **165**: p. 108401.
13. Lin, X., et al., *Deformation and cracking behaviors of proton-irradiated 308L stainless steel weld metal strained in simulated PWR primary water.* Journal of Materials Science & Technology, 2022. **120**: p. 36-52.
14. Ming, H., et al., *Microstructure, local mechanical properties and stress corrosion cracking susceptibility of an SA508-52M-316LN safe-end dissimilar metal weld joint by GTAW.* Materials Science and Engineering: A, 2016. **669**: p. 279-290.
15. Brooks, J. and A. Thompson, *Microstructural development and solidification cracking susceptibility of austenitic stainless steel welds.* International Materials Reviews, 1991. **36**(1): p. 16-44.
16. Jiao, Z. and G. Was, *Novel features of radiation-induced segregation and radiation-induced precipitation in austenitic stainless steels.* Acta Materialia, 2011. **59**(3): p. 1220-1238.
17. Brager, H. and F. Garner, *Swelling as a consequence of gamma prime (γ') and M23 (C, Si) 6 formation in neutron irradiated 316 stainless steel.* Journal of Nuclear Materials, 1978. **73**(1): p. 9-19.

18. Maziasz, P., *Formation and stability of radiation-induced phases in neutron-irradiated austenitic and ferritic steels.* Journal of Nuclear Materials, 1989. **169**: p. 95-115.
19. Kanematsu, K., *Stability of Crystal Structure of (Fe, V) 3M and (Fe, Ni) 3M (M= Si, Ge, Sn) and Its Analysis Based on Rigid Band Model.* Transactions of the Japan institute of metals, 1986. **27**(4): p. 225-232.
20. Li, Z., *Surface hardening of austenitic Fe-Cr-Ni alloys for accident-tolerant nuclear fuel cladding*. 2018, Case Western Reserve University. p. 155.
21. Toyama, T., et al., *Irradiation-induced precipitates in a neutron irradiated 304 stainless steel studied by three-dimensional atom probe.* Journal of nuclear materials, 2011. **418**(1-3): p. 62-68.
22. Krummeich, R., et al., *Solute cluster formation in austenitic and ferritic alloys under ion irradiation: a three‐dimensional atom probe characterization.* Surface and Interface Analysis: An International Journal devoted to the development and application of techniques for the analysis of surfaces, interfaces and thin films, 2004. **36**(5‐6): p. 575-580.
23. Li, Z., et al., *Irradiation response of delta ferrite in as-cast and thermally aged cast stainless steel.* Journal of Nuclear Materials, 2015. **466**: p. 201-207.
24. Kong, B.S., et al., *Effect of proton irradiation on δ-ferrite in the thermally aged austenitic stainless steel weld: Precipitation of G-phase and additional hardening.* Journal of Nuclear Materials, 2021. **544**: p. 152656.
25. Jiao, Z., J. Hesterberg, and G. Was, *Effect of post-irradiation annealing on the irradiated microstructure of neutron-irradiated 304L stainless steel.* Journal of Nuclear Materials, 2018. **500**: p. 220-234.
26. Lin, X., et al., *Irradiation-induced segregation at phase boundaries in austenitic stainless steel weld metal.* Scripta Materialia, 2018. **149**: p. 11-15.
27. Mansur, L., *Theory and experimental background on dimensional changes in irradiated alloys.* Journal of Nuclear Materials, 1994. **216**: p. 97-123.
28. Ziegler, J.F., *The stopping and range of ions in matter*, in *http://srim.org/*. 2013.
29. Chen, Y., P.H. Chou, and E.A. Marquis, *Quantitative atom probe tomography characterization of microstructures in a proton irradiated 304 stainless steel.* Journal of Nuclear Materials, 2014. **451**(1-3): p. 130-136.
30. Stephenson, L.T., et al., *New techniques for the analysis of fine-scaled clustering phenomena within atom probe tomography (APT) data.* Microscopy and Microanalysis, 2007. **13**(6): p. 448-463.
31. Malis, T., S. Cheng, and R. Egerton, *EELS log‐ratio technique for specimen‐thickness measurement in the TEM.* Journal of electron microscopy technique, 1988. **8**(2): p. 193-200.
32. Kolenda, M., et al., *Magnetic properties of Mn6Ni16Si7 and Mn3Cr3Ni16Si7.* Journal of magnetism and magnetic materials, 1991. **96**(1-3): p. 121-124.
33. Niu, H. and I. Chang, *Microstructural evolution during laser cladding of M2 high-speed steel.* Metallurgical and Materials Transactions A, 2000. **31**(10): p. 2615-2625.
34. Was, G. S., and J. T. Busby. "Role of irradiated microstructure and microchemistry in irradiation-assisted stress corrosion cracking." Philosophical Magazine 85, no. 4-7 (2005): 443-465.

35. Busby, J. T., G. S. Was, and E. A. Kenik. "Isolating the effect of radiation-induced segregation in irradiation-assisted stress corrosion cracking of austenitic stainless steels." Journal of Nuclear Materials 302, no. 1 (2002): 20-40.